International Journal of Heat and Mass Transfer 132 (2019) 1250–1261

Contents lists available at ScienceDirect

International Journal of Heat and Mass Transfer

journal homepage: www.elsevier.com/locate/ijhmt

Multi-objective heat transfer optimization of 2D helical micro-fins using NSGA-II

Garrett W. Mann [b,*], Steven Eckels [a]

[a] Institute for Environmental Research, 920N 17th St. 56 Seaton Hall, Manhattan, KS 66506, United States
[b] Mann Engineering Consulting, 115 Carnegie Pl., Pittsburgh, PA 15208, United States

ARTICLE INFO

Article history:
Received 11 January 2018
Received in revised form 12 December 2018
Accepted 12 December 2018
Available online 19 December 2018

Keywords:
Heat transfer
Enhancement
Micro-fin
Optimization
NSGA-II

ABSTRACT

A numerical simulation of helical micro-fins is implemented in ANSYS Fluent 15. The model is scripted to automatically set up and execute given three input parameters: fin height, helix angle, and number of starts. The simulation results reasonably predict experimental pressure drop and heat transfer for multiple micro-fin geometries. A multi-objective parameter optimization is implemented based on the NSGA-II algorithm to estimate the optimal trade-off (Pareto front) between Nusselt number and friction factor of a micro-fin tube for $0.0006 < e/D < 0.045$, $10 < N_s < 70$, at Reynolds number of 49,013. The resulting Pareto front is analyzed and compared with several experimental data points. From the optimal results, a distinct difference in flow characteristics was identified between geometries above and below a helix angle of approximately 45°. How the Pareto front can be used to choose micro-fin geometries for different performance evaluation criterion scenarios is demonstrated. Optimal results from various existing correlations are also compared to the optimization results.

1. Introduction

Numerical simulations of heat transfer and fluid flow over heat transfer surfaces not only allow satisfactory design and insight into local flow physics without expensive or impossible experimentation but also parameter optimization. Optimization via simulation poses various problems. Due to the significant computational cost of each simulation, performing this type of optimization for most heat transfer surfaces is very time consuming. This issue is compounded by the fact that heat transfer systems often have conflicting objectives that tend to be application specific. Thus, the optimum for one system may not be broadly applicable to many different design scenarios.

One way to produce optimization results that are more general is to consider the problem explicitly as a multi-objective optimization. The goal of such a problem is to find the Pareto front—the set of all non-dominated solutions. A solution is non-dominated if there are no other feasible solutions that can improve one of the objectives without diminishing another. The Pareto front thus represents all possible optimal solutions over the design space and can be computed without selecting the relative importance of the objectives. The front may then be used by the designer to chose the best parameters for various system applications without needing to re-run the optimization.

Multi-objective optimization is typically carried out using evolutionary algorithms. These have the benefits of being naturally parallel, of robustly accommodating failed geometry generation or diverging solutions, and of not requiring a gradient of the cost function(s). Common multi-objective optimization genetic algorithms (MOGA) are the non-dominated sorting genetic algorithm II (NSGA-II) [1] and the strength Pareto evolutionary Algorithm 2 (SPEA2) [2].

MOGAs have been applied to entire heat exchangers in several studies including optimization of shell-and-tube [3–7], compact [8–10], fin and tube [11], and plate heat exchangers [12–14], all of which use some form of correlation to evaluate the objectives. These algorithms have also been applied to surface-level optimization—optimization of the geometry of fluid-facing surfaces at a local level. Problems of this scope do not encompass such a wide range of scales as whole-heat exchanger optimization. Thus, studies can be found evaluating the objectives using higher-accuracy computational fluid dynamics (CFD) simulation. Examples of this are Hilbert et al. [15] and more recently Ranut et al. [16] with tube shape optimization; Cavazzuti and Corticelli [17] and Nobile et al. [18] with 2D plate heat exchanger passage optimization; Foli et al. with micro heat exchangers [19]; and Copiello and Fabbri with fin optimization [20].

* Corresponding author.
E-mail addresses: gmann@mann-consulting.net (G.W. Mann), eckels@ksu.edu (S. Eckels).

https://doi.org/10.1016/j.ijheatmasstransfer.2018.12.078
0017-9310/

One class of heat exchanger surfaces that have been neglected for multi-objective optimization, or any formal optimization beyond parameter studies, is in-tube micro-fins. Micro-fin surfaces often are one of the key components of chiller shell-and-tube evaporators and condensers, which are widely produced and utilized. Because of the wide use of these devices, even small improvements in performance would result in significant energy savings. These surfaces also are typically on the single-phase side of a heat exchanger. Commonly, the overall heat transfer coefficient for a heat exchanger is limited by this surface. Additionally, manufacturing advances are enabling shorter fins and closer fin spacing. The wide parameter ranges enabled could greatly benefit from optimization to drive more complex surface design.

Micro-fin tubes have been studied experimentally, though discrepancies exist between the data sets. The main findings of the experimental works are the following. For micro-fins, the transition region persists to higher Reynolds numbers, not becoming fully developed until $Re \approx 20,000$ [21]. At high Reynolds numbers, correlation with Reynolds number is similar to that of a smooth tube, but significant enhancements are realized, with larger fin height, pitch, and helix angle generally causing higher heat transfer and friction factor [22]. The effects of these parameters are interrelated. However, in the transition region, a direct influence may not always be present. Many correlations exist including these parameters([23,24] give reviews of correlations). The highest micro-fin heat transfer enhancements are approximately 4–4.1 with corresponding friction factor enhancement of 2.5–2.7 [22,25].

Micro-fins have also been studied numerically, although there are fewer works in this area. Different aspects of the modeling process have been emphasized in the literature. A range of periodic computational domains have been proposed, and multiple turbulence models have been tried including Spalart-Allmaras, Shear Stress Transport (SST), $k-\epsilon$ of Goldberg, $k-\epsilon$ of Lam-Bremhorst [26], $k-\epsilon$ of Norris and Reynolds [27,28], and the RNG $k-\epsilon$ [29–31]. One paper was found using large eddy simulation (LES) instead of a RANS turbulence model with excellent results [32]. These models have a range of accuracies with the best RANS models matching the experimental data within 11% for Nusselt number [26,33] and 4.5% for friction factor [31] and the LES model predicting within 3.7% and 4.2% respectively [32]. These simulations tended to predict well at high Reynolds numbers while significantly under-predicting friction factor at low Reynolds numbers because of the difficulty of modeling the turbulence near the wall. While some of these numerical studies sought to find the relationship between micro-fin geometry parameters and the heat transfer and pressure drop [28,29,31,34], this was done through simple parameters studies; no formal optimization algorithms were employed.

In this paper, fluid flow through a helical micro-fin tube is numerically modeled and used with a multi-objective optimization algorithm. The result of the optimization is the Pareto front showing the trade-off between optimal friction factor and Nusselt number over a wide range of fin height, number of starts, and helix angles. The flow patterns of the results are analyzed, and the bulk performance is compared to experimental data from the literature as well as Pareto fronts computed from existing correlations.

2. Problem description

2.1. Geometry

The geometry of a 2D micro-fin tube consists of fin profiles helically extruded along the interior of the tube. In this context, "2D" designates that the fin profile is two dimensional which, along with the helix specifications, completely specifies the geometry. Two dimensional micro-fins contrast from 3D micro-fins which are cross-cut along the helical path to make the fins disconnected axially (e.g. [35]). The main parameters describing the geometry are helix angle (α), fin height (e), and number of starts (N_s) around the tube perimeter, which is related to the axial fin pitch by

$$p = \frac{\pi D}{N_s \tan(\alpha)}, \tag{1}$$

where D is the diameter of the tube. Following the tubes in [36], a trapezoidal fin profile was chosen which is defined geometrically by the included angle of the fin (β) and the fin tip width (t). Fig. 1 illustrates these dimensions.

2.2. Design space and constraints

It is well recognized that the three most significant geometry variables for micro-fins are fin height, helix angle, and number of starts ([22,28]). Liu and Jensen also demonstrated that fin width influences the results, though they showed that this parameter influenced the results less dramatically than the other three [28]. Numerical work by Bhatia and Webb [30] indicated very little effect of the fin shape on heat transfer or friction. Liu and Jensen showed numerically that triangle and rectangular fin shapes yielded almost identical results, but round profiles differed from rectangular fin profiles at certain Reynolds numbers [28]. The design variables were thus chosen to be fin height, helix angle, and number of starts, with fixed fin profile ($\beta = 41^\circ$), fin width (t = 0.12 mm), and diameter (D = 15.54 mm) based on the tubes in [36]. Reynolds number was considered for inclusion as a design variable, but to reduce the requirements of the automatic mesh generator and to give results that were more easily interpreted, Reynolds number was fixed. The range of these design variables was

$$0.01 < e < 0.7 \text{ mm} \tag{2}$$

$$0 < \alpha < 60^\circ \tag{3}$$

$$10 < N_s < 70. \tag{4}$$

The range is wide enough to capture the transition between the major flow mechanisms. The span of e gives a maximum e/D of 0.045, which is well above the range of micro-fins given by [22] of $e/D = 0.03$. The range of α is wide enough to encompass flows that should recirculate and reattach, at least for sufficiently small N_s as suggested by [37]. The range of N_s is large enough that for certain α, flow recirculation between the fins could result. In addition, combinations within this range encompasses both small and large surface area enhancements.

Not all combinations of the above variables are geometrically feasible. In particular, too many starts with fins that are too high will lead to intersecting fins. Thus, instead of a rectangular prism design space, a section is cut out as shown in Fig. 2. Appendix A derives the relationship between critical fin height and number of starts.

2.3. Objectives

The two objectives were chosen to be the following:

$$\mathrm{f}_1 = \left.\frac{f}{f_s}\right|_{Re} \tag{5}$$

$$\mathrm{f}_2 = \left.\frac{Nu}{Nu_s}\right|_{Re} \tag{6}$$

where Nu and Nu_s are the Nusselt numbers of an enhanced and smooth tube respectively and the f and f_s are the fanning friction factor of an enhanced and smooth tube respectively. The first objective, f_1, is minimized, and f_2 is maximized. Both of these are

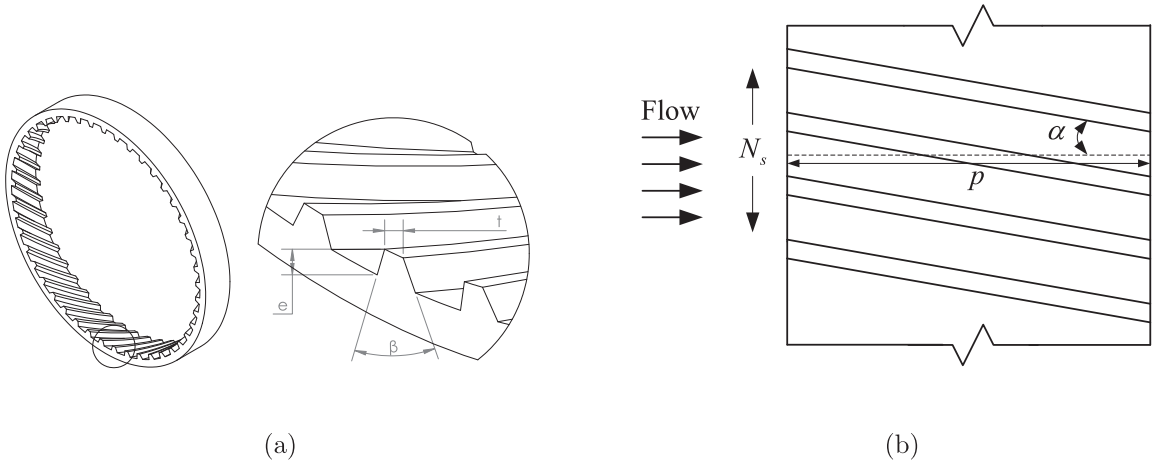

Fig. 1. Geometry parameter definitions.

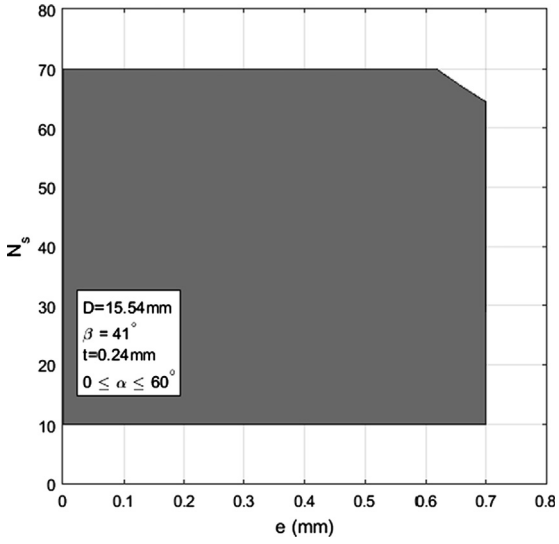

Fig. 2. Design space constraint between N_s and e.

evaluated at the same Reynolds number. The smooth tube friction factor was evaluated using the Petukhov equation, and the smooth tube Nusselt number was evaluated with the Gnielinski equation [38].

Webb and Kim in [39] discuss the concept of performance evaluation criteria (PEC) for heat exchangers. Depending on the desired performance, design constraints, or allowable geometry modification in a heat exchanger, the enhancement in heat transfer can be applied in different ways. They list twelve different configurations of constraints and objectives for utilizing the enhancement as an improvement over a smooth tube heat exchanger. In four of these configurations, the Reynolds number of the smooth and enhanced tubes stays the same. These cases are FG-1 (maximizing heat transfer or minimizing temperature difference with surface area and flow rate constant), FN-1 (minimizing heat exchanger length with fixed flow rate, pumping power, and heat transfer duty), FN-2 (minimizing heat exchanger length with fixed flow rate and heat transfer duty with pumping power free), and FN-3 (minimizing pumping power with fixed flow and heat transfer duty). With the objectives from (5) and (6), each of these four PEC cases can be directly solved from the Pareto front by enumerating the value to be optimized for each member of the Pareto set and then choosing the optimal one. This is demonstrated in Appendix B. Selection can be done without re-generating the Pareto front, allowing broad applicability and usefulness of the optimization results. To the authors' knowledge, an explicit demonstration of how PEC cases can be evaluated using the Pareto front has never before been documented. Future work is necessary to extend this technique to the remaining eight cases.

3. Simulation setup

3.1. Domain

A domain long enough to directly yield fully developed flow in a tube this size would require a very large mesh, which would be computationally prohibitive considering the many of simulations that will be performed in this study. Thus, translationally periodic boundary conditions were used on the inlet and outlet of the tube to allow the use of a significantly smaller domain. Periodicity for pressure is achieved by deconstructing the pressure profile into linearly-decreasing (constant over the entire domain) and spatially variable portions. Only the variable pressure profile is actually periodic along the pipe. The variable portion is solved as the normal pressure in the RANS equations; the linearly-decreasing portion is iteratively solved as a body force to produce the desired mass flow rate. Similarly, translational periodicity for the energy equation is transformed to a dimensionless temperature variable θ:

$$\theta = \frac{T\left(\vec{r}\right) - T_{wall}}{T_{bulk,inlet} - T_{wall}}, \tag{7}$$

where $T_{bulk,inlet}$ and $T\left(\vec{r}\right)$ are the bulk temperature at the domain inlet and the local temperature at any point in the domain respectively. This variable is translationally periodic for a domain with constant wall temperature.

Thus, the domain consisted of a thin, axial slice of the tube (see Fig. 3). The length of the slice was determined by a series of tests evaluating the convergence of the results. Since the periodic boundary condition in Fluent requires the inlet and outlet face meshes to only differ by a pure translation, the domain lengths were chosen such that the inlet and outlet were rotated an integer number of fins from each other (i.e. L must be integer multiples of p). Note that this constraint means that the domain lengths for geometries with different helix angles or number of starts will be different. It was found that if the offset was only equal to one fin rotation, the solution did not converge. Thus, lengths of two, four, and six fin rotations were evaluated. Table 1 shows the results

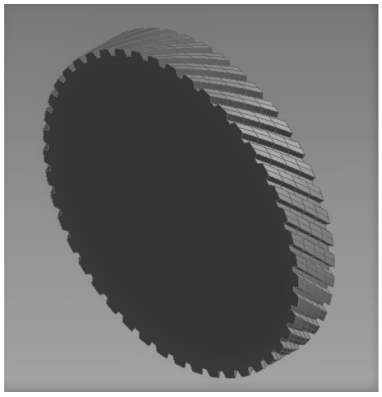

Fig. 3. Computational domain.

Table 1
Results of domain length study. Differences are with respect to six rotations.

Re	Length	*f*	Diff (%)	*Nu*	Diff (%)
19,685	2	0.0117	0.29	335.0	0.31
19,685	4	0.0117	0.11	334.3	0.10
19,685	6	0.0117	–	334.0	–
31,381	2	0.0115	0.14	495.6	0.07
31,381	4	0.0115	0.02	495.2	−0.01
31,381	6	0.0115	–	495.3	–
49,012	2	0.0107	−3.69	682.9	0.37
49,012	4	0.0109	−0.22	680.3	−0.02
49,012	6	0.0110	–	680.4	–

from the simulations with varying length. All of the results were consistent within 1% except the friction factor at the highest Reynolds number which showed a 3.7% deviation from the six fin rotation. Despite this difference, the additional computational cost that would be required to use a four fin rotation was deemed not to be worth the additional accuracy, and the two fin rotation was selected.

3.2. Flow rate

An initial study on the ability of the simulation to predict friction and heat transfer for variations in Reynolds number produced the results shown in Fig. 4. These results show that while the model predicts well for heat transfer and friction factor at high Reynolds numbers, the prediction is poor at low Reynolds numbers. This is similar to the findings of [40] and is due to the laminarization that persists to high Reynolds number but that is difficult for turbulence models to capture. Due to this fact, a high Reynolds number ($Re = 49,013$ from a round mass-flow number) was chosen for the optimization.

Ji et al. plot Nu/Pr^n and f versus Reynolds number for all the main experimental helical micro-fin works from the literature [25]. They show that for high enough Reynolds number (the fully rough region, $Re > 30,000$) both friction factor and the Nusselt number are approximately proportional to $Re^{0.8}$. This observation has been also made elsewhere (e.g. [22]) Thus, f/f_s and Nu/Nu_s from this optimization study will be expected to hold for a range of Reynolds numbers throughout the fully rough region—perhaps a little lower, but certainly at higher Reynolds numbers than the chosen value.

3.3. Mesh

Due to the complex structure of the helical fins, an unstructured, tetrahedral mesh was selected away from the wall. Close to the wall, mesh inflation providing prism cells was applied to the wall boundaries with an inflation ratio of 1.2. Ultimately, eight inflation layers were used.

3.4. Properties and boundary conditions

The following modeling assumptions/parameters were used to simulate the flow in the domain:

- The flow was considered to be incompressible.
- The fluid was liquid water at 293.15 K (bulk, upstream temperature) and 1 atm.
- The thermodynamic and transport properties were constant ($\rho = 998.2$ kg/m^3), $\mu = 0.001003$ Pa s, $k = 0.6$ W/m K, $C_p = 4182$ J/kg K, and $Pr = 6.99$) evaluated using REFPROP [41,42] at 293.15 K and 1 atm.
- A steady state solver was used.
- The RANS equations were solved with the following turbulence models: realizable k-ϵ, k-ω, k-kl-ω, and Reynold's stress model (RSM). Details for these models are given under Model Validation.

As mentioned previously, boundary conditions on the upstream and downstream side of the pipe section were set to translationally

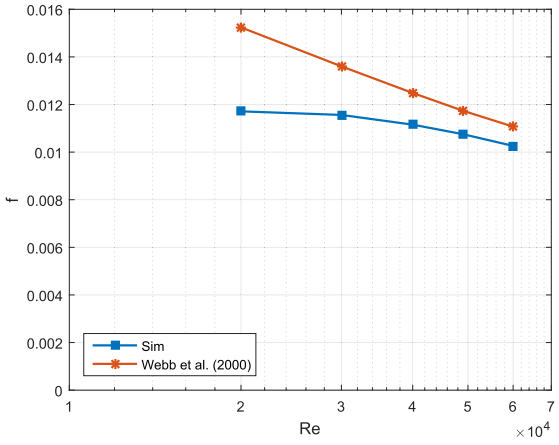

(a) f for different Reynolds numbers.

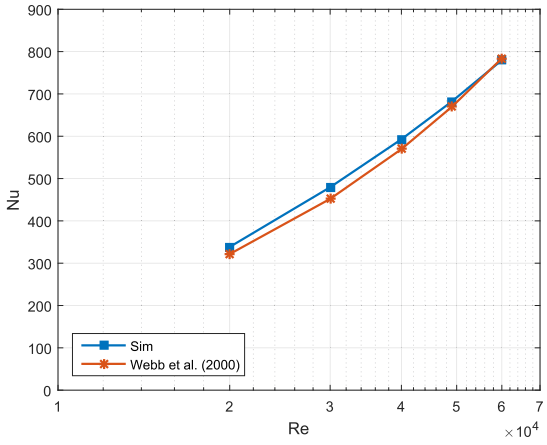

(b) Nu for different Reynolds numbers.

Fig. 4. Comparison of simulation (realizable $k-\epsilon$ turbulence model) with data from Webb et al. (2000), Tube 2.

periodic. No slip and constant temperature (at 25 K above bulk temperature for all cases) boundary conditions were applied at the domain walls. Constant temperature boundary conditions allowed for simpler post-processing than constant heat flux (an average wall temperature does not need to be defined) and should yield the same results as constant heat flux boundary condition since the properties were assumed constant with temperature. The wall surfaces were assumed to be hydraulically smooth.

3.5. Discretization and convergence

The discretization for pressure was second order. The discretization for momentum and energy was second order upwind. For turbulence parameters, the discretization was first order upwind. A least squares, cell-based gradient was used. The velocity and pressure equations were coupled in the solution process.

Convergence for the momentum equations was monitored by changes in the bulk pressure gradient from the periodic velocity domain scheme. The stop criterion limit was set to 10^{-6}, using the default ANSYS Fluent stop criterion scheme over the previous ten iterations: after each iteration, the maximum absolute variance for each of the previous ten pressure gradient values was divided by the pressure gradient from the current iteration to give ten residuals. If the maximum of these ten residuals was less than the defined limit, the solution was judged to be converged. Convergence for the energy equation was similarly monitored by changes in the integral of total heat flux over the pipe walls. The stop criterion limit was set to 10^{-6} over five previous iterations.

4. Data reduction

The two key parameters of interest from each simulation were Fanning friction factor (f) and average Nusselt number (Nu). These parameters were derived from the simulation results in the following way.

4.1. Friction factor

Because of the translationally periodic boundary condition, the simulation directly reported the average streamwise pressure gradient as a single value. This along with the mass flow rate, fluid properties, and tube geometry was used to compute the friction factor as

$$f = \frac{\frac{dP}{dz}\pi^2 R^5 \rho}{\dot{m}^2}, \tag{8}$$

where $\frac{dP}{dz}$ is the streamwise pressure gradient, R is the root radius of the tube, ρ is the density, and $\dot{m}$ is the mass flow rate. The formulation assumes that the bulk velocity of the flow is related to the mass flow rate by the *root* area rather than the true cross-sectional area. The affect of this assumption on the result will be minor due to the short fins.

4.2. Nusselt number

For Nusselt number (Nu), the heat transfer coefficient was first computed using

$$h = \frac{q''}{LMTD}\frac{A_w}{2\pi DL}, \tag{9}$$

where q'' is the average heat flux along the pipe wall, A_w is the true surface area of the wall, D and L are the root diameter and domain length of the pipe section respectively, and $LMTD$ is given by

$$LMTD = \frac{(T_w - T_i) - (T_w - T_o)}{\ln\left(\frac{T_w - T_i}{T_w - T_o}\right)}, \tag{10}$$

where T_i is the bulk average inlet temperature from the simulation results, T_w is the constant wall temperature specified in the simulation, and T_o is the outlet bulk temperature computed with

$$T_o = \frac{q'' A_w}{\dot{m} C_p} + T_i. \tag{11}$$

C_p is the heat capacity of the fluid. From the heat transfer coefficient, the Nusselt number is

$$Nu = \frac{hD}{k}, \tag{12}$$

where k is the thermal conductivity of the fluid, and D is the root diameter of the pipe.

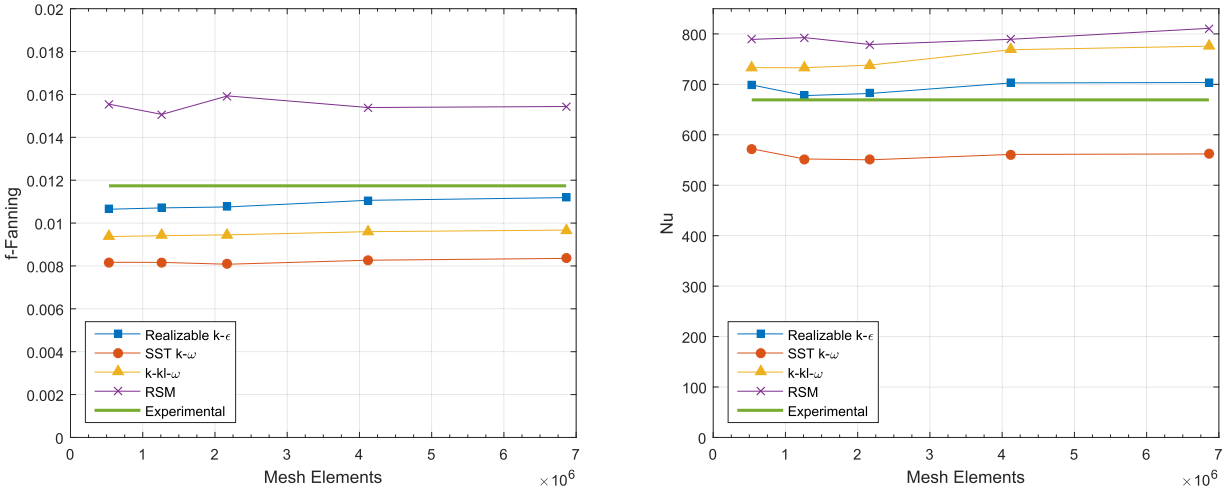

(a) f for different grid sizes and turbulence models (b) Nu for different grid sizes and turbulence models

Fig. 5. Turbulence model results for Tube 2.

5. Model validation

Results from four turbulence models were compared to find the most predictive for this problem. Possibilities were restricted to models already implemented in ANSYS Fluent 15. These models were the realizable $k-\epsilon$, SST $k-\omega, k-kl-\omega$ transition model, and Reynolds stress model (RSM). Each of these models have been described at length in other publications, so only a basic description with references will be given here.

This realizable formulation of the $k-\epsilon$ model was developed by [43] to ensure that the normal turbulent stress stays positive and that the Schwarz inequality is satisfied for large strain rates. When traditional wall functions are not employed, a two-layer model is implemented where the dissipation rate is computed from the algebraic model of Wolfshtein [44] in the region sufficiently close to the wall. The solver interpolates between the results from the Wolfshtein model and wall functions depending on the grid size allowing for grid independence studies to converge. The standard production limiter and low Reynolds number correction were used.

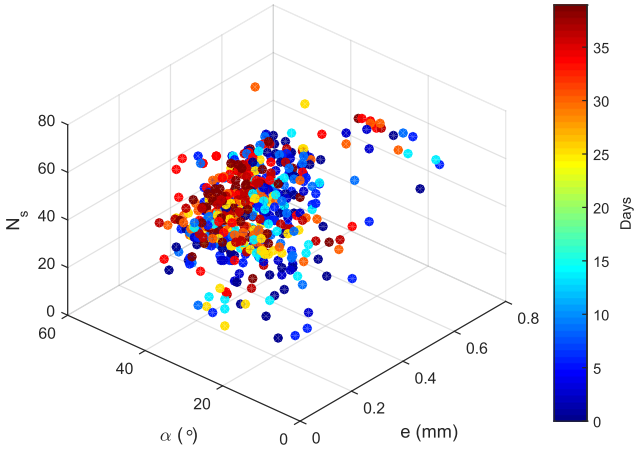

Fig. 7. Sampling of the design space over time.

Table 2
Simulation results for Tubes 2, 6, and 7.

Tube #	f_{sim}	f_{exp}	Diff (%)	Nu_{sim}	Nu_{exp}	Diff (%)
2	0.0108	0.01174	−8.4	669	703	1.9
6	0.00970	0.0110	−11.8	506	604	−16.3
7	0.00805	0.009025	−10.8	455	557	−18.8

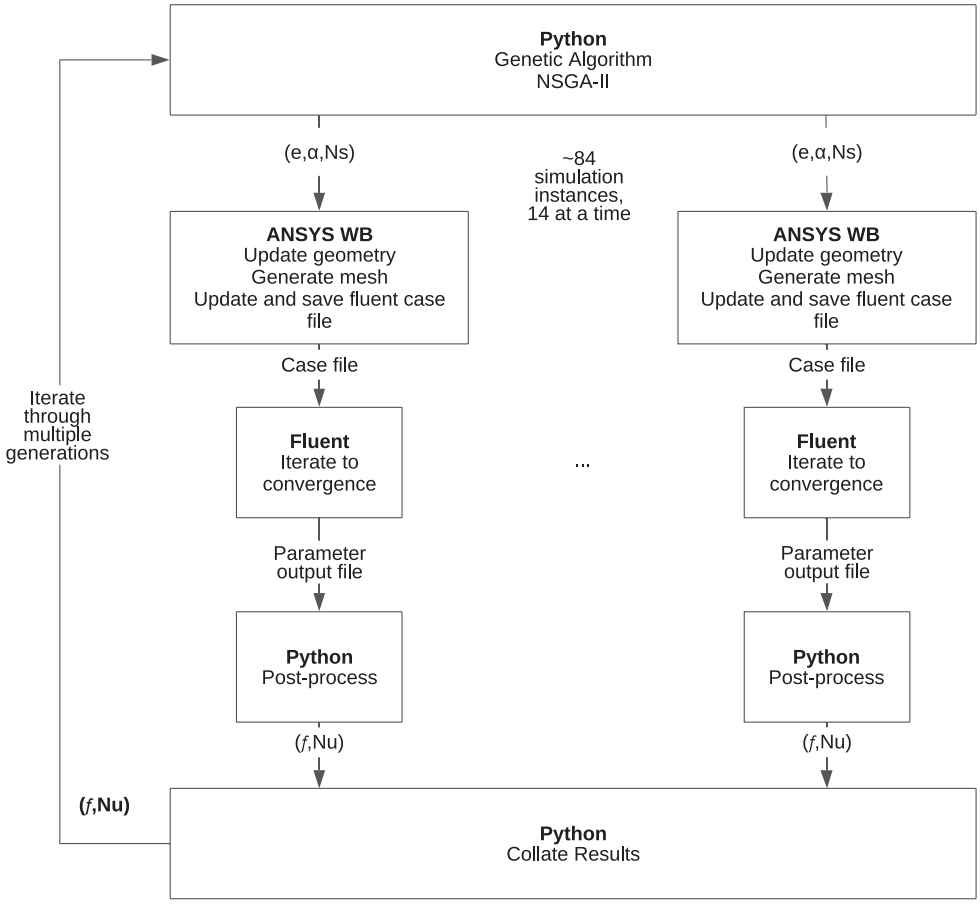

Fig. 6. Computational framework for optimization problem. For each generation, the population consisted of eighty-four simulation instances, taken fourteen at a time.

The $k-\omega$ turbulence model replaces the dissipation rate of the $k-\epsilon$ model with specific dissipation rate, resulting in better numeric stability close to the wall. The shear-stress transport (SST) modification blends the results from $k-\epsilon$ in the free stream with the $k-\omega$ formulation near the wall [45].

The $k-kl-\omega$ model is a three-equation model considering equations for turbulent kinetic energy, laminar kinetic energy, and the inverse turbulent time scale [46]. It was developed to model laminar transition to turbulence.

For each of the turbulence models, enhanced wall treatment was used, a formulation that smoothly switches between the law-of-the-wall solution for coarse meshes and the transport equation solution for fine meshes.

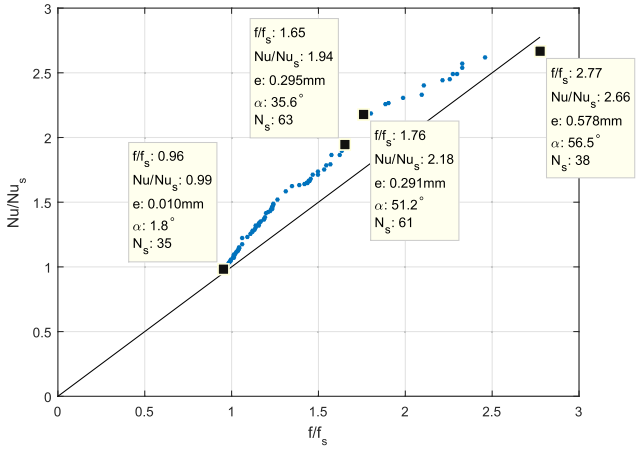

Fig. 8. The Pareto front after 10 generations.

Simulations with each of these turbulence models were performed for Tube 2 ($e=0.327, \alpha=45°, N_s=45$), Tube 6 ($e=0.430, \alpha=45°, N_s=10$) and Tube 7 ($e=0.430, \alpha=45°, N_s=10$) from Webb et al. [36], digitized (with [47]) and interpolated at Re = 49,013. In order to ensure an accurate comparison, for Tube 2, successively finer grids were used with each of the models to ensure grid convergence. The grid size was changed by increasing the number of inflation layers as well as decreasing the maximum allowable element size for the whole domain. For all of the simulations except for the coarsest grid, y^+ was less than 1.

Fig. 5 shows friction factor and Nusselt number versus grid size from simulations for Tube 2. It is apparent from this figure both that the SST $k-\omega$ and RSM models yield poor agreement with the experimental results. The SST $k-\omega$ model under-predicts both friction and heat transfer while the RSM model over-predicts them. Both the $k-\epsilon$ and $k-kl-\omega$ models give substantially closer results, but it is clear that the realizable $k-\epsilon$ is the closest.

Fig. 5 was also used to choose a standard grid density for the simulations. The 2.1 M element grid was chosen as a tradeoff between mesh size and solution accuracy. Table 2 compares friction factor and Nusselt number results at the chosen grid size for Tubes 2, 6, 7. These results were deemed to be close enough for the purposes of the optimization study.

6. Optimization algorithm

6.1. Genetic algorithm

Genetic algorithms are a set of numerical methods inspired by the biological theory of genetic evolution. A typical algorithm consists of a population of individuals that contain alleles (i.e.

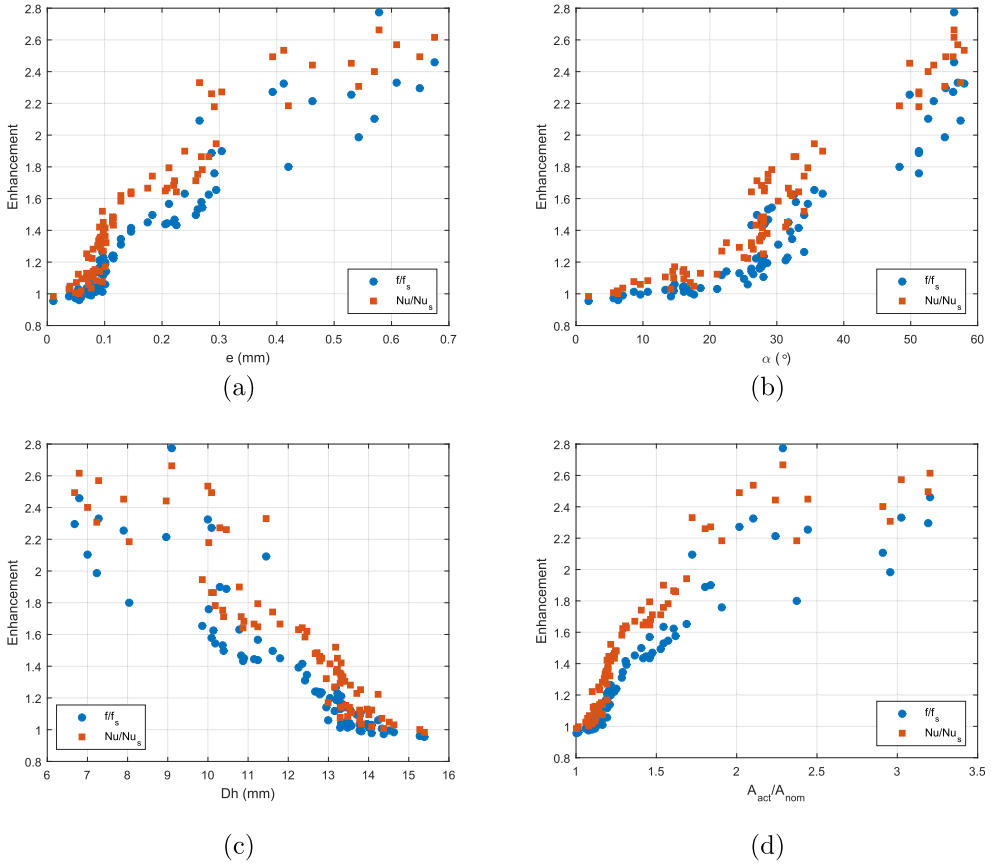

Fig. 9. Parameterization of Pareto front.

parameters) and a fitness value (i.e. objective). To form a successive generation, parents are selected from the population to produce offspring based on their fitness level. Additional mutation is performed on the alleles of the offspring individuals. Then based on the fitness of the offspring and parents, a new population is formed. As this process repeats, the individuals in the population converge towards the desired objective. For this study, the algorithm used for the multi-objective optimization was the non-dominated sorting genetic algorithm II (NSGA-II). This was developed by Deb et al. [1]. It uses a crowding operator along with Pareto dominance to rank different individuals in the population, forcing the individuals in successive generations to converge toward and spread out along the Pareto front.

The implementation used in this study used tournament selection (with tournament size of 2), blend crossover with a 10% blend rate, and Gaussian mutation with 10% rate of mutation from a standard normal distribution. All non-dominated individuals from all generations were archived to yield the best estimate of the Pareto front; the result of the algorithm is that archive.

6.2. Computational architecture

Fig. 6 depicts the information flow and computational architecture for the optimization algorithm. The optimization algorithm NSGA-II was used with the implementation from the *inspyred* python library [48]. For each generation, the eighty-four individuals in the population were evaluated/simulated in parallel fourteen at a time. The solver for each instance was parallelized by sixteen processes, thus 224 cores were used simultaneously in the computation. Individual simulations that failed due to meshing or convergence were removed from the algorithm by assigning unrealistically bad objective values. Thus, the parameters from those simulations were not propagated to the next generation.

7. Results and discussion

After a lengthy debugging period, the NSGA-II algorithm with micro-fin simulations was run for ten generations. Prior to the testing period, the algorithm was initialized with uniform sampling from the design space. The best results from the testing period were used to seed the original population of the final ten generations, thus speeding convergence. Ten generations were completed in 37 days of computation with an average of 3.4 days per generation. The total number of unique evaluations performed over these ten generations was 799. Of these geometries, 21% failed to either mesh or to converge in the solver.

Fig. 7 shows how the design space was sampled during the algorithms' progress. The samples are color-coded by time. While the samples are for the most part evenly distributed throughout the design space, no points are present at high helix angle and low fin heights, and at low number of starts, few points are present at high fin heights. While it is possible that these poorly sampled regions are due to failed geometries, it is more likely that the initial population was derived from the best candidates from the test

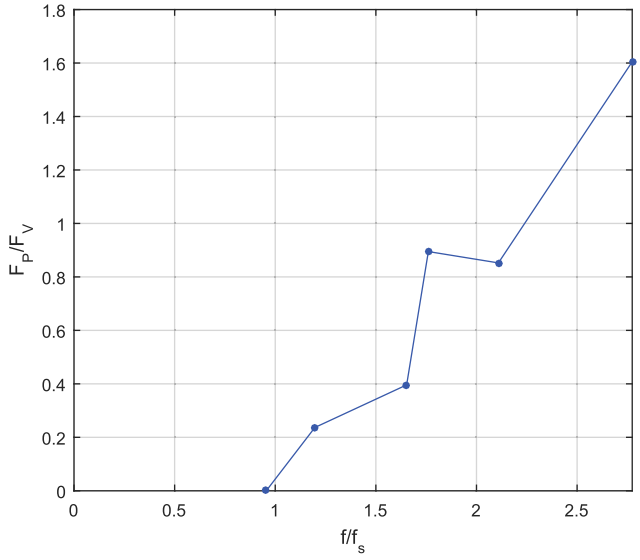

Fig. 11. Ratio of form drag to viscous drag for six geometries along the Pareto front.

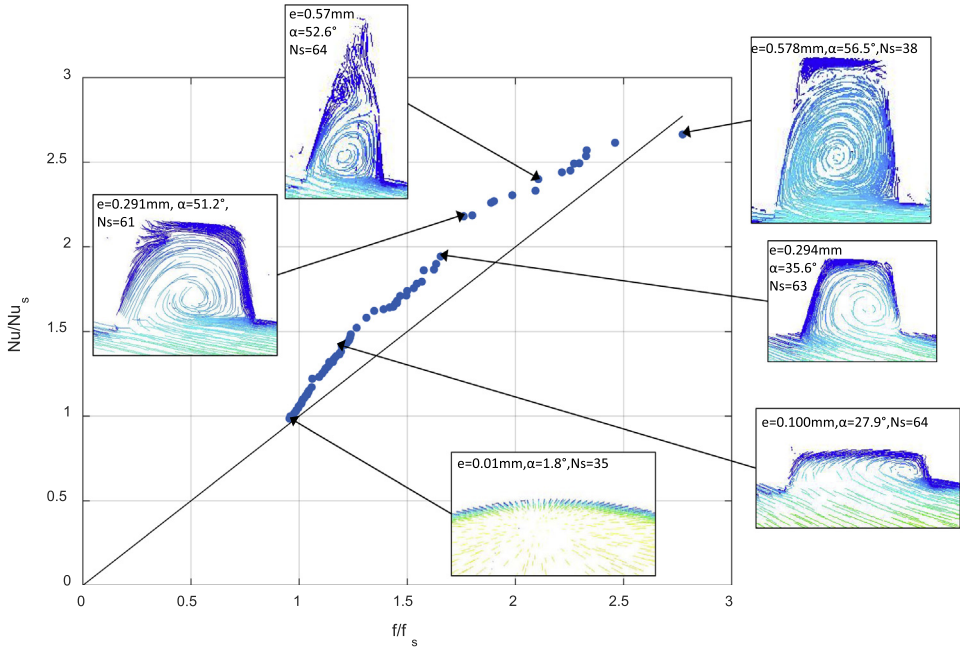

Fig. 10. Pareto front showing streamlines in gap between fins.

runs. The regions are sparse because they did not produce optimal values of heat transfer and friction.

Fig. 8 shows the final archived Pareto front [dataset] [49] (note: this is the final *archive* not the final *population*). There were 80 data points in this set at the conclusion of the 10th generation. The Pareto front demonstrates the expected behavior, stretching from close to the smooth tube results upward with convexity towards better heat transfer. The convexity indicates that certain geometry combinations produced greater than unity efficiency (more heat transfer enhancement than increase in friction factor). As the heat transfer enhancement gets higher, the cost to enhance it becomes greater, causing the front to curve back across the unity line at the upper end.

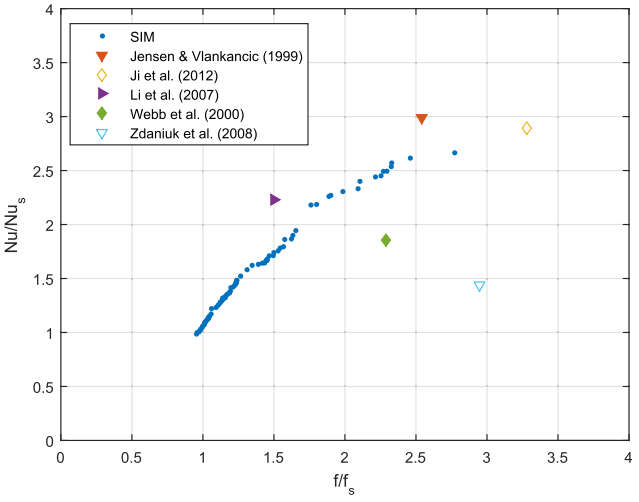

Fig. 12. Comparison of experimental data with optimal results at Re = 49,013.

Fig. 9 shows the relationship between four different parameters and the enhancement from these optimal points. There is a strong correlation between each of these four parameters (fin height, helix angle, hydraulic diameter, and area enhancement) and the enhancement level, especially for the lower region. For the upper portion, the relationship is more chaotic with certain parameter combinations yielding better or worse enhancement. Of particular interest from these plots is the relationship with helix angle, which shows a distinct break in the data around $\alpha \approx 45^{\circ}$. This indicates a change in flow characteristic. The region of lower helix angles correspond to a smooth regime where helix angle increase directly increases the local heat transfer coefficient and friction. Thus, in this regime, increase of helix angle results in a smooth increase in heat transfer and friction, likely coming from increasing turbulence production. However, in the upper regime, the front is no longer parametrized by smooth changes in helix angle, indicating a more chaotic flow with diverse combinations of geometry interacting with the turbulence along with area enhancement to bring about the increased heat transfer.

Fig. 10 show streamlines for six of the geometries along the front. The orientation of the geometry is so that into the page is along the fin valley—the geometry is rotated by the helix angle. These streamlines demonstrate that the two regimes are also distinguished by the presence of secondary vortices in the deepest portion of the fin valley. Those in the lower region only have a single vortex in the fin valley and thus have greater similarity between geometries with slightly different helix angles. Significantly, the geometry with the highest efficiency corresponds to the first appearance of this second helix, when the flow no longer

Table 3
Micro-fin correlations from the literature.

Notation	Authors	Expression	Reference
WNT_{PL}	Webb et al. (2000)	$f = 0.108Re^{-0.283}N_s^{0.221}\frac{e}{D}^{0.785}\alpha^{0.78}$ $Nu = 0.00933Re^{0.819}N_s^{0.285}\left(\frac{e}{D}\right)^{0.323}\alpha^{0.505}Pr^{1/3}$	[36]
WNT_{e+}	Webb et al. (2000)	$\sqrt{2/f} = B(e^+) - 2.5\ln(2e/D) - 3.75$ $Nu = \frac{(f/2)RePr}{1+\sqrt{f/2}\left(\bar{g}(e^+)Pr^{0.57}-B(e^+)\right)}$ $B(e^+) = 4.762(e^+)^{0.2138}N_s^{-0.1096}\alpha^{-0.297}$ $\bar{g}(e^+) = 1.714(e^+)^{0.06}N_s^{-0.21}\alpha^{-0.16}$ $e^+ = \frac{e}{D}Re\sqrt{f/2}$	[36]
RB	Ravigururajan et al. (1986)	$\frac{f}{f_s} = \left(1 + \left(29.1Re^a\left(\frac{e}{D}\right)^b\left(\frac{p}{D}\right)^c(\alpha/90)^d\left(1+\frac{2.94}{n}\right)\sin\left(\frac{\pi}{2}+\frac{\beta}{2}\right)\right)^{15/16}\right)^{16/15}$ $a = 0.67 - 0.06\frac{p}{D} - 0.49\frac{\alpha}{90}$ $b = 1.37 - 0.157\frac{p}{D}$ $c = -1.66\times10^{-6}Re - 0.33\frac{\alpha}{90}$ $d = 4.59 + 4.11\times10^{-6}Re - 0.15\frac{p}{D}$ n is number of corners facing the flow $Nu = \left(1 + \left(2.64Re^{0.036}\left(\frac{e}{D}\right)^{0.212}\left(\frac{p}{D}\right)^{-0.21}(\alpha/90)^{0.29}Pr^{-0.024}\right)^7\right)^{1/7}$	[50]
ZCW	Zdaniuk et al. (2008)	$f = 0.128Re^{-0.305}N_s^{0.235}\left(\frac{e}{D}\right)^{0.319}\alpha^{0.397}$ $Nu = 0.029Re^{0.653}N_s^{0.253}\left(\frac{e}{D}\right)^{0.0877}\alpha^{0.362}Pr^{1/3}$	[51]
JV	Jansen et al. (1999)	$\frac{f}{f_s} = \left(\frac{l_c}{D}\right)^{-1.25}\left(\frac{A_n}{A_c}\right)^{1.75} - \left(\frac{0.0151}{f_s}\right)\left(\left(\frac{l_c}{D}\right)^{-1.25}\left(\frac{A_n}{A_c}\right)^{1.75} - 1\right)\exp(-Re/6780)$ $\frac{Nu}{Nu_s} = \left(\frac{l_c}{D}\right)^{-0.5}\left(\frac{A_n}{A_c}\right)^{0.8}\left(\frac{P}{\pi D\cos(\alpha)}\right)\left[1 - 0.059\left(\frac{N_s\sin(\alpha)}{\pi}\right)^{-0.31}\left(\left(\frac{\pi}{N_s} - \frac{s}{D}\right)\cos(\alpha)\right)^{-0.66}\right]$ $s = \frac{A_n - A_c}{N_s e}$ $A_c = \frac{\pi D^2}{4}$ A_n is the actual flow area. P is the wetted perimeter. $\frac{l_c}{D} = \begin{cases} 1 - 1.577\left(\frac{N_s\sin(\alpha)}{\pi}\right)^{0.64}\left(\frac{2e}{D}\right)^{0.53}\left[\left(\frac{\pi}{N_s} - \frac{s}{D}\right)\cos(\alpha)\right]^{0.28} & \frac{2e}{D} < 0.04 \\ 1 - 0.994\left(\frac{N_s\sin(\alpha)}{\pi}\right)^{0.89}\left(\frac{2e}{D}\right)^{0.44}\left[\left(\frac{\pi}{N_s} - \frac{s}{D}\right)\cos(\alpha)\right]^{0.41} & 0.04 < \frac{2e}{D} < 0.06 \end{cases}$	[22]

appears to be smoothly related to helix angle. This is likely the point where the break-up of the flow is inducing high turbulence, but form drag is still lower. Fig. 11 corroborates this phenomena, showing the ratio of pressure drag to viscous drag for each of the six geometries from Fig. 10. This figure shows how the form drag jumps between the two regions (about f/f_s of 1.6) and then dramatically increases as the fins and helix angle grow in the upper regime.

In the review paper by Ji et al. [25], the main experimental works for heat transfer and friction factor in micro-fin tubes were reviewed. These data, interpolated to the same Reynolds number, are plotted with the optimal results in Fig. 12. The comparison indicates that the Pareto front out-performs some, but not all of the experimental data sets.

For an additional comparison, several well-known micro-fin correlations were implemented, and the Pareto front using these correlations was computed. Table 3 lists the different correlations that were considered. Fig. 13 shows the Pareto fronts for the four different correlations along with the simulation data (SIM). From this figure, it is apparent that for most of the correlations, in the lower enhancement region, the correlations show more favorable results than those from the simulation—i.e. the front is further to the left of the SIM front. For Webb et al. [36] power law (WNTpl), Ravigurajan & Bergles [50] (RB), and Zandiuk et al. [51] (ZCW), the unity crossover point occurs at a lower enhancement value than for the simulation. This perhaps indicates that the power law correlations are not able to adequately model the performance of the tubes for higher enhancement levels. Interestingly, the e^+ correlation of Webb et al. matches the simulation results well. This potentially indicates that the form of this correlation more closely matches the physics of the system then the power law models. Jansen & Vlakancic's [22] more detailed geometric model only matches at low enhancement levels. At the extremes, there is a significant discrepancy, with the JV correlation predicting a much higher efficiency than all the other correlations.

A review of the design parameters for the various geometries on the correlation fronts indicate somewhat unrealistic values. The optimization algorithm is pushing the correlation function into unrealistic regions. Other discrepancies could be due to differences in parameter ranges of databases, the errors in the underlying experimental data of the correlations, or errors due to grid spacing or turbulence model in the simulations.

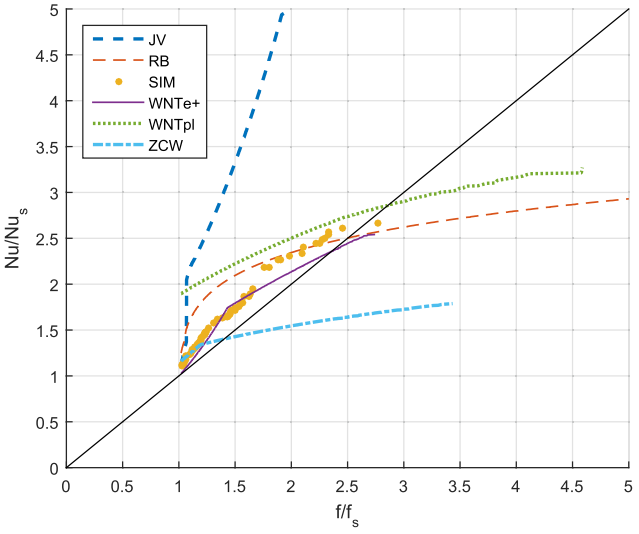

Fig. 13. Pareto front comparison between correlations and simulation results.

8. Conclusions

In this paper, a multi-objective optimization was performed for 2D helical micro-fin surfaces by CFD simulation. Fin height, helix angle, and number of starts were varied to find the Pareto front of two objectives—minimum friction enhancement and maximum heat transfer enhancement. The best results from 799 simulation evaluations were presented and compared to available data. Besides the results being significant from a design perspective, the results from the archival set indicate that for lower enhancement levels, small increases in helix angle and fin height smoothly increase heat transfer and friction. At the higher enhancement levels, for helix angles greater than 45°, there is consistently a double vortex in-between the fins, and the relationship between heat transfer enhancement and geometry is chaotic rather than smooth. In addition, Pareto fronts computed from correlations were compared to the simulation Pareto front. This comparison indicated that most of the correlations over-predicted the performance of the simulation. The power law correlations show particularly poor prediction. The list of optimal geometries are included as attached data for the use of micro-fin designers or for seeding future optimization studies.

Admittedly, the utilization of the optimal results from this study are limited by the high Reynolds number. Such a high Reynolds number was chosen due to the difficultly of predicting micro-fin performance at lower Reynolds numbers. However, this paper demonstrates the feasibility and potential of the multi-optimization approach. Future work will include a repeat of the computations for lower Reynolds numbers.

Funding

This project was internally funded by the Institute for Environmental Research.

Author declarations

The authors declared that there is no conflict of interest.

Acknowledgments

The authors are grateful for Matthew Campbell's input on this paper and his review of the final manuscript.

Appendix A. Derivation of N_s constraint

The geometric parameters defining the geometry of the micro-fins are not geometrically independent. High fins with too many starts will cause the fins to intersect. This appendix briefly derives the constraint between the number of starts (N_s) and the fin height (e).

Fig. A.1 gives the geometry of half of a fin and defines the relevant variables for the derivation. As is shown, as the fin gets wider by the increase of e, t, or β, it will eventually outgrow its allotted sector ($\frac{\pi}{N_s}$) and intersect with the neighboring fin. Thus the constraint to prevent this is

$$\xi + \theta < \frac{\pi}{N_s} \tag{A.1}$$

It remains then to find expressions for ξ and θ in terms of the geometry definition parameters (e, t, β) and root radius (R). Notice first that sector D can decomposed into two right triangles which gives the relationship:

$$\tan\frac{\xi}{2} = \frac{t}{4(R-e)}. \tag{A.2}$$

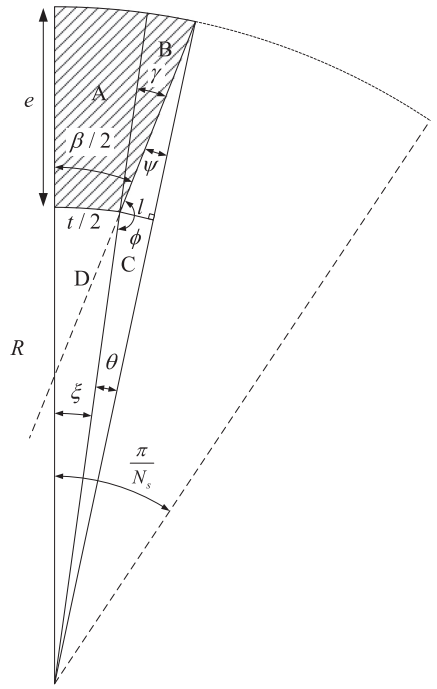

Fig. A.1. Fin geometry for constraint derivation.

This rearranged yields

$$\xi = 2\tan^{-1}\left(\frac{t}{4(R-e)}\right). \tag{A.3}$$

Careful inspection gives an expression for γ:

$$\gamma = \frac{\beta}{2} - \xi. \tag{A.4}$$

For ϕ,

$$\phi = \pi - \gamma \tag{A.5}$$

$$\phi = \pi - \left(\frac{\beta}{2} - \xi\right). \tag{A.6}$$

By the law of sines,

$$\frac{R}{\sin\phi} = \frac{R-e}{\sin\psi} \tag{A.7}$$

$$\psi = \sin^{-1}\left(\frac{(R-e)\sin(\phi)}{R}\right). \tag{A.8}$$

Finally,

$$\theta = \pi - \phi - \psi. \tag{A.9}$$

Substituting and simplifying this leads to

$$\xi + \theta = \xi + \pi - \left(\pi - \left(\frac{\beta}{2} - \xi\right)\right) - \psi \tag{A.10}$$

$$\xi + \theta = \frac{\beta}{2} - \psi \tag{A.11}$$

$$\xi + \theta = \frac{\beta}{2} - \sin^{-1}\left(\frac{(R-e)\sin(\phi)}{R}\right). \tag{A.12}$$

The inequality constraint on N_s is then from (A.1)

$$N_s < \pi\left[\frac{\beta}{2} - \sin^{-1}\left(\frac{(R-e)\sin\left(\frac{\beta}{2} - 2\tan^{-1}\left(\frac{t}{4(R-e)}\right)\right)}{R}\right)\right]^{-1}. \tag{A.13}$$

Appendix B. Application of Pareto front to different performance evaluation criteria scenarios

This appendix shows how the results from the non-dominated set (Pareto front) can be used to obtain the best micro-fin geometries for four different PEC cases. The nomenclature for the PEC cases is from [39].

B.1. FG-1

In this configuration, maximum heat transfer (or alternatively minimum temperature difference) is sought for fixed nominal surface area (number of tubes and exchanger length) and flow rate. No constraint is placed on the pumping power. The ratio of heat transfer of enhanced versus smooth tube is

$$\frac{Q}{Q_s} = \frac{hA\Delta T_{lm}}{h_s A_s \Delta T_{lm}} \tag{B.1}$$

Maximizing the heat transfer or minimizing the ΔT_{lm} is equivalent to maximizing $\frac{h}{h_s}$ (since $\frac{A}{A_s} = 1$). Thus, the best geometric configuration is given by the maximum f_2 in the Pareto set. In the discussion, $f_1 = f/f_s$ and $f_2 = Nu/Nu_s$ from (6).

B.2. FN-1

In this configuration, minimum heat exchanger length is desired for fixed flow rate, frontal area, heat transfer duty and pumping power. The pumping power constraint can be written as

$$\frac{P}{P_s} = \frac{f}{f_s}\frac{A}{A_s}\left(\frac{G}{G_s}\right)^3 = 1 \tag{B.2}$$

Due to the fixed frontal area and flow rate constraint, this simplifies to a constraint on $\frac{f}{f_s}$:

$$\frac{f}{f_s} = \frac{A_s}{A} \tag{B.3}$$

Similarly, the constraint on the heat transfer coefficient (from above) is

$$\frac{Nu}{Nu_s} = \frac{A_s}{A} \tag{B.4}$$

Eliminating $\frac{A}{A_s}$ gives

$$\frac{Nu}{Nu_s} = \frac{f}{f_s} \tag{B.5}$$

Thus, the optimal geometry can be found by the intersection of the constraint ($f_2/f_1 = 1$) with the Pareto front. Since there may be multiple locations on the Pareto front where this condition holds, the optimal value is the one farthest from the origin.

B.3. FN-2

For this configuration, the objective is minimum heat exchanger length as before, but pumping power is allowed to vary. Because of this, only (B.4) applies. Thus the optimal value is the largest value of f_2 on the Pareto front.

B.4. FN-3

For this configuration, the objective is minimum pumping power. Substituting (B.4), the pumping power is

$$\frac{P}{P_s} = \frac{f}{f_s}\frac{Nu_s}{Nu} \tag{B.6}$$

Thus, the maximum of f_2/f_1 (maximum efficiency) should be found by computing this quantity for each point on the Pareto front and numerically computing the maximum.

References

[1] K. Deb, A. Pratap, S. Agarwal, T. Meyarivan, A fast and elitist multi-objective genetic algorithm: NSGA-II, IEEE Trans. Evol. Comput. 6 (2) (2002) 182–197.
[2] E. Zitzler, M. Laumanns, L. Thiele, SPEA2: Improving the strength Pareto evolutionary algorithm, Tech. rep., Eidgenössische Technische Hochschule Zürich (ETH), Institut für Technische Informatik und Kommunikationsnetze (TIK), 2001.
[3] S. Fettaka, J. Thibault, Y. Gupta, Design of shell-and-tube heat exchangers using multiobjective optimization, Int. J. Heat Mass Transf. 60 (2013) 343–354.
[4] A. Agarwal, S.K. Gupta, Jumping gene adaptations of NSGA-II and their use in the multi-objective optimal design of shell and tube heat exchangers, Chem. Eng. Res. Des. 86 (2) (2008) 123–139.
[5] M.A. Elsays, M. Naguib Aiy, A.A. Badawi, Design optimization of shell-and-tube heat exchangers using single objective and multi-objective particle swarm optimization, Kerntechnik 75 (1–2) (2010) 38–46.
[6] H. Hajabdollahi, P. Ahmadi, I. Dincer, Exergetic optimization of shell-and-tube heat exchangers using NSGA-II, Heat Transf. Eng. 33 (7) (2012) 618–628.
[7] S. Sanaye, H. Hajabdollahi, Multi-objective optimization of shell-and-tube heat exchangers, Appl. Therm. Eng. 30 (14–15) (2010) 1937–1945.
[8] H. Hajabdollahi, M. Tahani, M.H.S. Fard, CFD modeling and multi-objective optimization of compact heat exchanger using CAN method, Appl. Therm. Eng. 31 (14–15) (2011) 2597–2604.
[9] P. Ahmadi, H. Hajabdollahi, I. Dincer, Cost and entropy generation minimization of a cross-flow plate fin heat exchanger using multi-objective genetic algorithm, J. Heat Transf. 133 (2) (2011), 021801–021801–10.
[10] S. Sanaye, H. Hajabdollahi, Thermal-economic multi-objective optimization of plate fin heat exchanger using genetic algorithm, Appl. Energy 87 (6) (2010) 1893–1902.
[11] D. Juan, Q.Z. Qin, Multi-objective optimization of a plain fin-and-tube heat exchanger using genetic algorithm, Therm. Eng. (Engl. Transl. Teploenergetika) 61 (4) (2014) 309–317.
[12] W. Han, K. Saleh, V. Aute, G. Ding, Y. Hwang, R. Radermacher, Numerical simulation and optimization of single-phase turbulent flow in Chevron-type plate heat exchanger with sinusoidal corrugations, HVAC R Res. 17 (2) (2011) 186–197.
[13] H. Lee, K. Saleh, Y. Hwang, R. Radermacher, Optimization of novel heat exchanger design for the application to low-temperature lift heat pump, Energy 42 (1) (2012) 204–212.
[14] J. Lee, K.S. Lee, Correlations and shape optimization in a channel with aligned dimples and protrusions, Int. J. Heat Mass Transf. 64 (2013) 444–451.
[15] R. Hilbert, G. Janiga, R. Baron, D. Thévenin, Multi-objective shape optimization of a heat exchanger using parallel genetic algorithms, Int. J. Heat Mass Transf. 49 (15–16) (2006) 2567–2577.
[16] P. Ranut, G. Janiga, E. Nobile, D. Thévenin, Multi-objective shape optimization of a tube bundle in cross-flow, Int. J. Heat Mass Transf. 68 (2014) 585–598.
[17] M. Cavazzuti, M.A. Corticelli, Optimization of heat exchanger enhanced surfaces through multiobjective genetic algorithms, Numer. Heat Transf. Part A: Appl. 54 (6) (2008) 603–624.
[18] E. Nobile, F. Pinto, G. Rizzetto, Geometric parameterization and multiobjective shape optimization of convective periodic channels, Numer. Heat Transf. Part B: Fundam. 50 (5) (2006) 425–453.
[19] K. Foli, T. Okabe, M. Olhofer, Y.C. Jin, B. Sendhoff, Optimization of micro heat exchanger: CFD, analytical approach and multi-objective evolutionary algorithms, Int. J. Heat Mass Transf. 49 (5–6) (2006) 1090–1099.
[20] D. Copiello, G. Fabbri, Multi-objective genetic optimization of the heat transfer from longitudinal wavy fins, Int. J. Heat Mass Transf. 52 (5–6) (2009) 1167–1176.
[21] H.K. Tam, L.M. Tam, A.J. Ghajar, C. Sun, H.Y. Leung, Experimental investigation of the single-phase friction factor and heat transfer inside the horizontal internally micro-fin tubes in the transition region, in: ASME-JSME-KSME 2011 Joint Fluids Engineering Conference, American Society of Mechanical Engineers, 2011, pp. 2963–2970.
[22] M.K. Jensen, A. Vlakancic, Experimental investigation of turbulent heat transfer and fluid flow in internally finned tubes, Int. J. Heat Mass Transf. 42 (7) (1999) 1343–1351.
[23] G.J. Zdaniuk, L.M. Chamra, P.J. Mago, Experimental determination of heat transfer and friction in helically-finned tubes, Exp. Therm. Fluid Sci. 32 (3) (2008) 761–775.
[24] A. Celen, A.S. Dalkilic, S. Wongwises, Experimental analysis of the single phase pressure drop characteristics of smooth and microfin tubes, Int. Commun. Heat Mass Transf. 46 (2013) 58–66.
[25] W.-T. Ji, A.M. Jacobi, Y.-L. He, W.-Q. Tao, Summary and evaluation on single-phase heat transfer enhancement techniques of liquid laminar and turbulent pipe flow, Int. J. Heat Mass Transf. 88 (2015) 735–754.
[26] J.H. Kim, K.E. Jansen, M.K. Jensen, Simulation of three-dimensional incompressible turbulent flow inside tubes with helical fins, Numer. Heat Transf. Part B: Fundam. 46 (3) (2004) 195–221.
[27] X.Y. Liu, M.K. Jensen, Numerical investigation of turbulent flow and heat transfer in internally finned tubes, J. Enhanced Heat Transf. 6 (2–4) (1999) 105–119.
[28] X.Y. Liu, M.K. Jensen, Geometry effects on turbulent flow and heat transfer in internally finned tubes, J. Heat Transf.-Trans. ASME 123 (6) (2001) 1035–1044.
[29] R.S. Bhatia, R.L. Webb, Numerical study of turbulent flow and heat transfer in micro-fin tubes—part 1, model validation, J. Enhanced Heat Transf. 8 (5) (2001) 291–304.
[30] R.S. Bhatia, R.L. Webb, Numerical study of turbulent flow and heat transfer in micro-fin tubes—part 2, parametric study, J. Enhanced Heat Transf. 8 (5) (2001) 305–314.
[31] W. Li, P. Fu, H. Li, G. Li, P. Thors, Numerical-theoretical analysis of heat transfer, pressure drop, and fouling in internal helically ribbed tubes of different geometries, Heat Transf. Eng. 37 (3–4) (2016) 279–289.
[32] Z. Hernádi, G. Kristóf, Prediction of pressure drop and heat transfer coefficient in helically grooved heat exchanger tubes using large eddy simulation, Proc. Inst. Mech. Eng., Part A: J. Power Energy 228 (2013) 317–327.
[33] P. Jasiński, Numerical study of friction factor and heat transfer characteristics for single-phase turbulent flow in tubes with helical micro-fins, Arch. Mech. Eng. 59 (4) (2012) 469–485.
[34] P. Jasiński, Numerical optimization of flow-heat ducts with helical micro-fins, using entropy generation minimization (EGM) method, in: Proceedings of WSEAS International Conferences (HTE'11), 2011, pp. 47–54.
[35] Q. Liao, X. Zhu, M. Xin, Augmentation of turbulent convective heat transfer in tubes with three-dimensional internal extended surfaces, J. Enhanced Heat Transf. 7 (3) (2000) 139–151, https://doi.org/10.1615/JEnhHeatTransf.v7.i3.10.
[36] R.L. Webb, R. Narayanamurthy, P. Thors, Heat transfer and friction characteristics of internal helical-rib roughness, J. Heat Transf.—Trans. ASME 122 (1) (2000) 134–142.
[37] R. Webb, E. Eckert, R. Goldstein, Heat transfer and friction in tubes with repeated-rib roughness, Int. J. Heat Mass Transf. 14 (4) (1971) 601–617.
[38] T.L. Bergman, F.P. Incropera, Fundamentals of Heat and Mass Transfer, seventh ed., John Wiley, Hoboken, NJ, 2011.
[39] R. Webb, N. Kim, Principles of Enhanced Heat Transfer, Taylor & Francis Group, 2005.
[40] J.-H. Kim, K.E. Jansen, M.K. Jensen, Analysis of heat transfer characteristics in internally finned tubes, Numer. Heat Transf. Part A: Appl. 46 (1) (2004) 1–21.
[41] E.W. Lemmon, M.L. Huber, M.O. McLinden, NIST Standard Reference Database 23: Reference Fluid Thermodynamic and Transport Properties—REFPROP, Version 9.1, National Institute of Standards and Technology, 2013. <https://www.nist.gov/srd/refprop>.
[42] W. Wagner, A. Pruß, The IAPWS formulation 1995 for the thermodynamic properties of ordinary water substance for general and scientific use, J. Phys. Chem. Ref. Data 31 (2) (2002) 387–535.
[43] T.H. Shih, W.W. Liou, A. Shabbir, Z. Yang, J. Zhu, A new k-ϵ eddy-viscosity model for high Reynolds number turbulent flows—model development and validation, Comput. Fluids 24 (1995) 227–238.
[44] M. Wolfshtein, The velocity and temperature distribution in one-dimensional flow with turbulence augmentation and pressure gradient, Int. J. Heat Mass Transf. 12 (3) (1969) 301–318.
[45] F.R. Menter, Two-equation eddy-viscosity turbulence models for engineering applications, AIAA J. 32 (8) (1994) 1598–1605.
[46] D.K. Walters, D. Cokljat, A three-equation eddy-viscosity model for Reynolds-averaged Navier-Stokes simulations of transitional flow, J. Fluids Eng. 130 (12) (2008) 121401.
[47] A. Rohatgi, WebPlotDigitizer, <http://arohatgi.info/WebPlotDigitizer/app>.
[48] A. Garrett, inspyred. <https://pythonhosted.org/inspyred/>.
[49] G. Mann, S. Eckels, Data for: multi-objective heat transfer optimization of 2D helical microfins using NSGA-II, Mendeley Data (2018), https://doi.org/10.17632/hdzwfgftw3.1.
[50] T. Ravigururajan, A. Bergles, Study of water-side enhancement for ocean thermal conversion heat exchangers, Tech. Rep. HTL-44/ERI Project 1718, Iowa State University, 1986.
[51] G.J. Zdaniuk, L.M. Chamra, D.K. Walters, Correlating heat transfer and friction in helically-finned tubes using artificial neural networks, Int. J. Heat Mass Transf. 50 (23) (2007) 4713–4723.